

HIERARCHICAL FORMATION OF DARK MATTER HALOS AND THE FREE STREAMING SCALE

TOMOAKI ISHIYAMA

Center for Computational Science, University of Tsukuba, 1-1-1, Tennodai, Tsukuba, Ibaraki 305-8577, Japan; ishiyama@ccs.tsukuba.ac.jp

Received 2014 January 18; accepted 2014 April 6; published 2014 May 19

ABSTRACT

The smallest dark matter halos are formed first in the early universe. According to recent studies, the central density cusp is much steeper in these halos than in larger halos and scales as $\rho \propto r^{-(1.5-1.3)}$. We present the results of very large cosmological N -body simulations of the hierarchical formation and evolution of halos over a wide mass range, beginning from the formation of the smallest halos. We confirmed early studies that the inner density cusps are steeper in halos at the free streaming scale. The cusp slope gradually becomes shallower as the halo mass increases. The slope of halos 50 times more massive than the smallest halo is approximately -1.3 . No strong correlation exists between the inner slope and the collapse epoch. The cusp slope of halos above the free streaming scale seems to be reduced primarily due to major merger processes. The concentration, estimated at the present universe, is predicted to be 60–70, consistent with theoretical models and earlier simulations, and ruling out simple power law mass–concentration relations. Microhalos could still exist in the present universe with the same steep density profiles.

Key words: cosmology: theory– dark matter – Galaxy: structure – methods: numerical

Online-only material: color figures

1. INTRODUCTION

According to a concordance cold dark matter (CDM) theory, dark matter halos hierarchically evolve in an expanding universe. The smallest dark matter microhalos first undergo gravitational collapse, and then merge to form larger halos. The size of the smallest halo is determined by the free streaming scale of the dark matter particles. If dark matter comprises the lightest supersymmetric particle (the neutralino of mass approximately 100 GeV), a cutoff in the matter power spectrum of the very early universe should result from free streaming damping of this particle. The estimated corresponding mass of the smallest microhalos is approximately Earth-mass, 3.5×10^{-9} – $8.4 \times 10^{-6} M_{\odot}$ (Zybin et al. 1999; Hofmann et al. 2001; Berezhinsky et al. 2003; Green et al. 2004; Loeb & Zaldarriaga 2005; Bertschinger 2006; Profumo et al. 2006; Berezhinsky et al. 2008). However, this interval could be increased by uncertainty in supersymmetry theory.

If many Earth-mass microhalos exist in the present universe, they could significantly enhance gamma-ray signals by neutralino self-annihilation (Berezhinsky et al. 2003; Diemand et al. 2005; Berezhinsky et al. 2008; Ishiyama et al. 2010). Many studies have debated whether gamma-rays generated by neutralino annihilation in subhalos and microhalos are observable in indirect dark matter detection experiments (e.g., Berezhinsky et al. 2003; Koushiappas et al. 2004; Oda et al. 2005; Colafrancesco et al. 2006; Koushiappas 2006; Goerdt et al. 2007; Diemand et al. 2007a; Ando et al. 2008; Diemand et al. 2008; Kuhlen et al. 2008; Springel et al. 2008b; Lee et al. 2009; Giocoli et al. 2009; Ishiyama et al. 2010; Kamionkowski et al. 2010; Schneider et al. 2010; Charbonnier et al. 2011; Pieri et al. 2011; Belotsky et al. 2014; Blanchet & Laval 2012; Mack 2014; Ng et al. 2013). Since the gamma-ray flux is proportional to the square of the local dark matter density, the annihilation signal from the Milky Way halo should largely depend on the halo’s fine structure.

Analytic studies and cosmological simulations have predicted that the subhalo mass function scales as $dn/dm \propto m^{-(2-1.8)}$ (e.g., Berezhinsky et al. 2003; Ishiyama et al. 2009b), although no consensus has yet emerged. Thus, smaller subhalos are abundant

in the Milky Way, and some of them will probably pass near the Sun. The survivability of microhalos and larger subhalos in the Milky Way depends on their structure. This suggests that the structure of the smallest microhalos can determine the fine structure of the dark matter halo. Therefore, to evaluate the observable annihilation flux, we must understand the density structures of microhalos.

Historically, the structures of relatively large halos (galaxy-sized to cluster-sized) have been investigated by cosmological N -body simulations (e.g., Springel et al. 2008a; Diemand et al. 2008; Ishiyama et al. 2013). In most works, the structures of these halos follow the Navarro–Frenk–White (NFW) profile (Navarro et al. 1996) or the Einasto profile (Einasto 1965). In these profiles, the slopes of radial density profiles approximate -1 in the inner region, gradually increasing -3 toward the outer region. Some of the above cited studies have estimated the gamma-ray flux from microhalos assuming that microhalos follow these profiles. However, unlike massive halos that contain many subhalos, microhalos contain no subhalos by definition and do not form by hierarchical merging of smaller halos. Thus, the structure of microhalos may largely differ from that of larger halos.

The structure of microhalos was first investigated in numerical simulations performed by Diemand et al. (2005). They successfully fitted the density profiles of microhalos to the form, $\rho(r) \propto r^{-\gamma}$, where the slope γ ranges from 1.5 to 2, down to radii as low as $\sim 10^{-3}$ pc. However, the mass resolution in the simulation of Diemand et al. (2005) was $1.2 \times 10^{-10} M_{\odot}$, which is insufficient to resolve the central structures of microhalos.

Ishiyama et al. (2010) improved the mass and spatial resolutions in the earlier study by 100 and 20 times, respectively. After numerous simulations were performed at the higher resolution, they found that the central density cusps of microhalos scale much more steeply than those of larger halos, with $\rho \propto r^{-1.5}$. These results are supported by recent similar simulations (Anderhalden & Diemand 2013), in which inner profiles scale as $\rho \propto r^{-(1.4-1.3)}$.

Such steep cusps in the density profile may largely impact on indirect experimental searches for dark matter. The

contribution of microhalos, based on the density profiles derived from cosmological simulations, are estimated in Diemand et al. (2005), Ishiyama et al. (2010), and Anderhalden & Diemand (2013). However, their estimation relies on results of only a few simulated halos. Statistical study, such as the distribution of microhalo density profiles, requires a more extensive data set. Ishiyama et al. (2010) analytically estimated that the formation epoch of microhalos is affected by larger scale density fluctuations. They predicted that the formation epoch of their simulated microhalos was later than the average value. Since halo concentration reflects the cosmic density at which halos collapse, this suggests that their microhalos were less concentrated than indicated by the average. Therefore, to precisely predict the gamma-ray flux, the distribution of both the microhalo density profile shapes and of microhalo concentrations must be elucidated.

The statistics are most effectively improved by simulating larger simulation boxes with uniform mass resolution and unbiasedly analyzing all halos. Although we can now simulate halos with ultra-high resolution by re-simulation method, selection bias is difficult to eliminate, and impedes the acquisition of good statistical samples of microhalos.

Another difficulty is resolving the free streaming scale with sufficient resolution. Two-body relaxation introduces numerical artifacts that significantly reduce the central density of microhalos. Artificial fragmentation can occur at filaments below the free streaming scale, as seen in warm dark matter simulations (Wang & White 2007; Schneider et al. 2013; Angulo et al. 2013). To avoid such numerical artifacts and obtain good statistics of well-resolved halos, substantially many particles are required. Such large simulations are numerically challenging and consume huge computational resources.

Despite these difficulties, such simulations are worthy of attempt, since they provide microhalo statistics and yield valuable structural information on halos, whose masses exceed Earth-mass by a few orders of magnitude. These halos are interesting targets since some of them are formed by mergers of microhalos. These halos could be structurally different from larger halos, and could resemble the smallest microhalos. Along with microhalos, these small halos may significantly contribute to the gamma-ray signal. The structural statistics of these halos may help to elucidate the mass scale at which the density profile transits to steeper cusps. Diemand et al. (2006) performed high-resolution simulations for a $0.014 M_\odot$ halo and analyzed it. However, there is only one halo, statistical study over a wide mass range is needed.

Another interesting point is that our simulations are closely related to warm dark matter simulations. Our simulations would give a huge opportunity to understand warm dark matter halos, since the cutoff in the matter power spectrum is imposed by a similar mechanism, although mass scales are largely different.

We address these questions by large and high-resolution cosmological N -body simulations. We present the first study of halo structure near the free streaming scale over a wide mass range. To reveal the statistics of these halos in the early universe, we simulated a large number of dark matter particles in sufficient volumes to reliably sample these halos. Section 2 describes our simulation method and its setup. The structures of halos near the free streaming scale, density profiles, profile distributions, dependence on the halo formation epoch, and halo evolution are presented in Section 3. The contributions of these halos to gamma-ray signals by neutralino self-annihilation

Table 1
Details of Simulations

Name	N	L (pc)	ε (pc)	m (M_\odot)	m_{DM} (GeV)
A_N4096L400	4096 ³	400.0	2.0×10^{-4}	3.4×10^{-11}	100
A_N4096L200	4096 ³	200.0	1.0×10^{-4}	4.3×10^{-12}	100
B_N2048L200	2048 ³	200.0	2.0×10^{-4}	3.4×10^{-11}	w/o cutoff

Note. Here, N , L , ε , M , and m_{DM} are the total number of particles, box length, softening length, mass resolution, and mass of dark matter particles, respectively.

is discussed in Section 4. The results are summarized in Section 5.

2. INITIAL CONDITIONS AND NUMERICAL METHOD

We performed three large cosmological N -body simulations. The cosmological parameters, namely, $\Omega_0 = 0.27$, $\lambda_0 = 0.73$, $h = 0.7$, and $\sigma_8 = 0.8$, were based on the concordance Λ CDM model (Komatsu et al. 2011). Two different initial matter power spectra were used. In two of the simulations, the power spectrum included the sharp cutoff imposed by the free streaming damping of dark matter particles with a mass of 100 GeV (Green et al. 2004). The third simulation ignored the effect of free streaming damping. We denote the former two simulations as model A, and the latter as model B. The initial conditions were generated by a first-order Zeldovich approximation at $z = 400$.

In the model A simulations (with the cutoff imposed), the motions of 4096³ particles in comoving boxes of side lengths 400 pc and 200 pc were followed (these simulations are denoted A_N4096L400 and A_N4096L200, respectively). The particle masses were $3.4 \times 10^{-11} M_\odot$ and $4.3 \times 10^{-12} M_\odot$, ensuring that halos at the free streaming scale were represented by $\sim 30,000$ and $\sim 230,000$ particles, respectively. Such high-resolution protects the halos from the artificial fragmentation as seen in warm dark matter simulations (Wang & White 2007; Schneider et al. 2013; Angulo et al. 2013). The respective gravitational Plummer softening lengths were 2.0×10^{-4} pc and 1.0×10^{-4} pc. The model B simulation (with no cutoff) followed the motions of 2048³ particles in comoving boxes of side length 200 pc (this simulation is denoted B_N2048L200). The particle mass was $3.4 \times 10^{-11} M_\odot$, and the gravitational Plummer softening length was 2.0×10^{-4} pc. Simulations A_N4096L400 and B_N2048L200 were performed at the same mass and spatial resolution, since both the number of particles and the simulated volume of simulation B_N2048L200 were one-eighth those of simulation A_N4096L400. To avoid unphysical density fluctuations at small scales (Colín et al. 2008), thermal velocities was not imposed in the initial conditions. The setup of the three simulations is detailed in Table 1.

Simulations were performed by massively parallel TreePM code, GreeM (Ishiyama et al. 2009a; Ishiyama et al. 2012)¹ on Aterui supercomputer at Center for Computational Astrophysics, CfCA, of National Astronomical Observatory of Japan, and the K computer at the RIKEN Advanced Institute for Computational Science. The calculation of the tree force was accelerated by the Phantom-GRAPE library² (Nitadori et al. 2006; Tanikawa et al. 2012, 2013) with support for AVX instruction set extension to the x86 architecture and the HPC-ACE architecture of the K computer. PM calculations of 4096³(2048³) particles

¹ <http://www.ccs.tsukuba.ac.jp/Astro/Members/ishiyama/greem>

² <http://code.google.com/p/phantom-grape/>

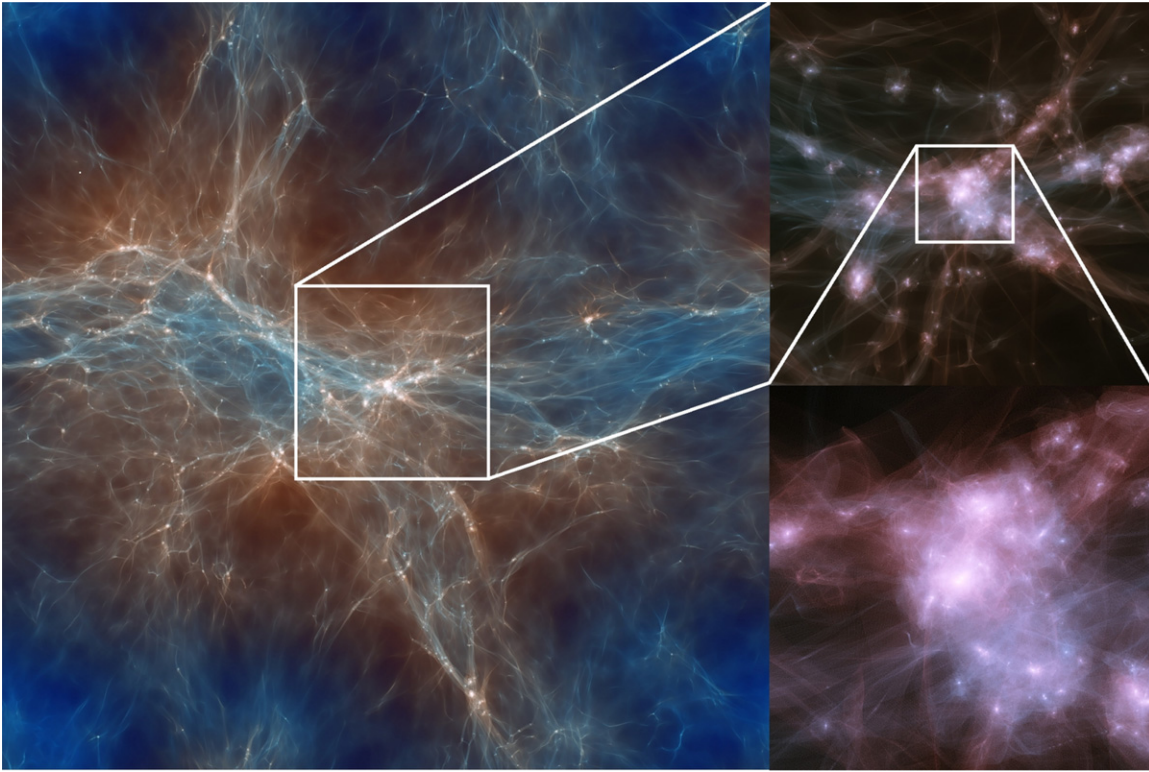


Figure 1. Distribution of dark matter in the A_N4096L200 simulation at $z = 32$, centered on the largest halo. The left panel shows the entire simulation volume. The right panels are enlargements of the largest halo. The widths of the left, top right, and bottom right images correspond to 400, 100, and 25 comoving pc, respectively. (A color version of this figure is available in the online journal.)

simulations were performed on $2048^3(1024^3)$ grid points and the opening angle for the tree method was 0.5. Simulations were terminated at $z = 32$, where long-wavelength perturbations comparable to the box size were no longer negligible.

Halos were identified by the spherical overdensity method (Lacey & Cole 1994). The virial radius of a halo r_{vir} is defined as the radius in which the spherical overdensity is $\Delta(z) = 18\pi^2 + 82x - 39x^2$ times the critical value, where $x \equiv \Omega(z) - 1$ (Bryan & Norman 1998). The virial mass of a halo M_{vir} is defined as the mass within the virial radius. The most massive halos identified in A_N4096L400, A_N4096L200, and B_N2048L200 simulations contained 170918717, 48316099, and 10505232 particles, respectively. The corresponding masses of these halos were $5.84 \times 10^{-3} M_{\odot}$, $2.08 \times 10^{-4} M_{\odot}$, and $3.59 \times 10^{-4} M_{\odot}$.

Figure 1 shows the dark matter distribution in the A_N4096L200 simulation at $z = 32$, centered on the largest halo. Several caustics are generated by nonlinear growth of long-wavelength perturbations. The distributions differ from those of large scale structure simulations, and are analogous to those obtained in warm dark matter simulations (e.g., Bode et al. 2001).

3. RESULTS

3.1. Density Profiles

We calculated the spherically averaged radial density profile of each halo within the range $0.02 \leq r/r_{\text{vir}} \leq 1.0$, divided into 32 logarithmically equal intervals. Each density profile deviates to varying extent from the average density profile, mainly because subhalos exist in the halos. To minimize this effect and obtain proper average radial density profiles of halos

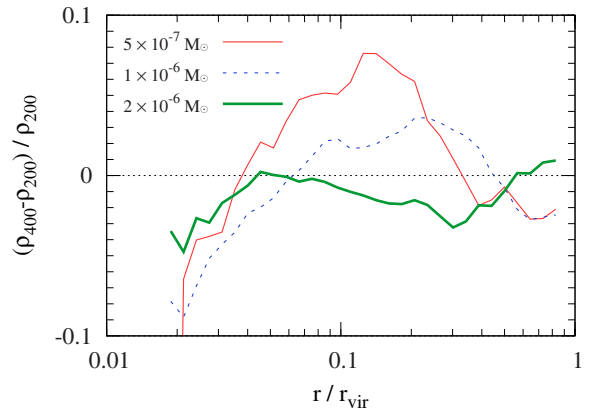


Figure 2. Residuals of stacked radial density profiles from simulation A_N4096L400 (ρ_{400}) to A_N4096L200 (ρ_{200}) as a function of radius (normalized by the virial radius). The mass resolution in the A_N4096L200 simulation is eight times higher than that of A_N4096L400. The results of three different mass bins are presented.

(A color version of this figure is available in the online journal.)

with a wide mass distribution, we stacked the profiles of similar-mass halos.

Halos resolved by a small number of particles suffer from numerical artifacts introduced by two-body relaxation. First, we evaluate the minimum mass that yields a reliable density profile. Figure 2 shows the normalized stacked density differences at $z = 32$ between the A_N4096L400 simulation and the A_N4096L200 simulation for halos of different masses ($5 \times 10^{-7} M_{\odot}$, $1 \times 10^{-6} M_{\odot}$ and $2 \times 10^{-6} M_{\odot}$). The density profile of the higher mass halo ($2 \times 10^{-6} M_{\odot}$) is almost identical in both simulations. The difference is below 5% within the radial range

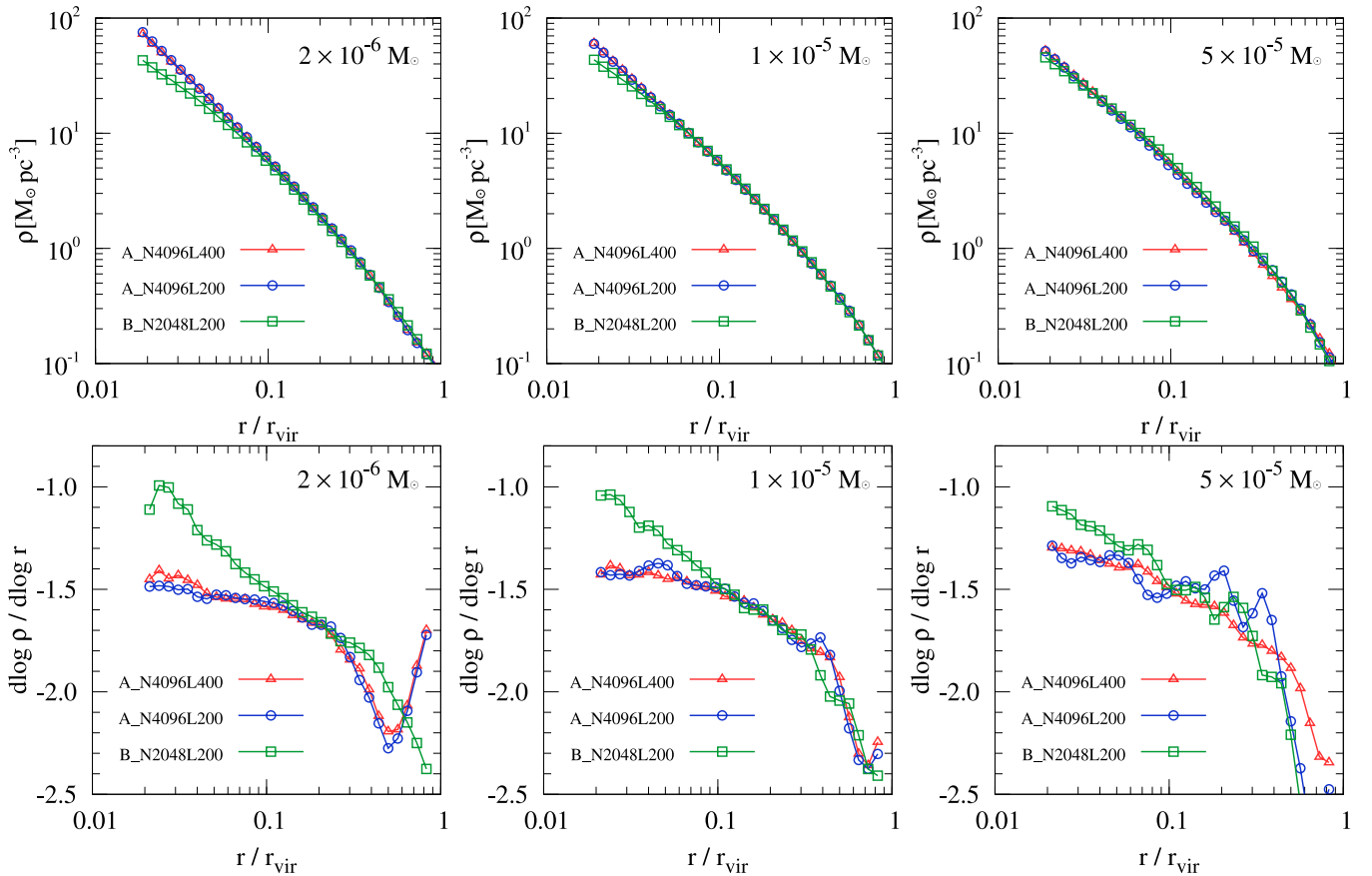


Figure 3. Stacked radial density profiles (top panel) and slopes of profiles (bottom panel) at $z = 32$ for three simulations as a function of radius (normalized by the virial radius).

(A color version of this figure is available in the online journal.)

$0.02 \leq r/r_{\text{vir}} \leq 1.0$. For the lower-mass halos ($5 \times 10^{-7} M_{\odot}$ and $1 \times 10^{-6} M_{\odot}$), poorer agreement between the simulations is observed across most ranges. The A_N4096L400 simulation yields smaller densities than the A_N4096L200 simulation from $\sim 0.05 r/r_{\text{vir}}$ and the difference is comparable to 10% at $0.02 r/r_{\text{vir}}$.

The mass resolution in the A_N4096L200 simulation is eight times higher than in the A_N4096L400 simulation. We infer that these density decreases are numerical artifacts introduced by two-body relaxation. Hereafter, we conservatively use the stacked density profiles of halos with the masses larger than $2 \times 10^{-6} M_{\odot}$ for the A_N4096L400 simulation and the B_N2048L200 simulation since both mass resolution are same.

Figure 3 shows the stacked radial density profiles of three simulations at $z = 32$ for three different mass bins, $2 \times 10^{-6} M_{\odot}$, $1 \times 10^{-5} M_{\odot}$, and $5 \times 10^{-5} M_{\odot}$. The density profiles of the A_N4096L400 and A_N4096L200 simulations show excellent agreement. However, large differences appear between the simulations with the cutoff (A_N4096L400 and A_N4096L200) and that without the cutoff (B_N2048L200). For halos of $2 \times 10^{-6} M_{\odot}$, the central cusps in the density profiles are substantially steeper when the cutoff is imposed. These results are consistent with those of earlier works (Ishiyama et al. 2010; Anderhalden & Diemand 2013). The effect of the cutoff is reduced in halos of higher mass ($1 \times 10^{-5} M_{\odot}$ and $5 \times 10^{-5} M_{\odot}$). These results are highlighted in the bottom panel of

Figure 3, which plots the local logarithmic slopes of the density profiles.

These surprising results are further highlighted in Figure 4. The stacked density profiles are plotted as in Figure 3, but each panel shows the density profiles of three different mass bins taken from the A_N4096L400 and B_N2048L200 simulations. With the cutoff imposed, the slope of the central cusp gradually shallows at higher masses. For halos of $2 \times 10^{-6} M_{\odot}$, the central slope is around $-1.5 \sim -1.4$, consistent with earlier reports (Ishiyama et al. 2010; Anderhalden & Diemand 2013). For $5 \times 10^{-5} M_{\odot}$ halos, the central slope is reduced to around -1.3 . Remarkably, the central slopes of density profiles are almost flat and tend toward a constant value at $r/r_{\text{vir}} \lesssim 0.04$.

Without the cutoff, the results are dramatically different. As seen in the right panels of Figure 4, the slopes of the density profile become shallower at inner radii and do not converge to a single power law. The shape of the inner density profile appears to be independent of halo mass, consistent with the results of cosmological simulations for galaxy-sized and cluster-sized halos (e.g., Fukushige et al. 2004; Stadel et al. 2009; Ishiyama et al. 2013).

Why the inner density profile becomes shallower toward the center in simulations without cutoff and of larger halos is not currently understood, and is not pursued further in this paper. In Section 3.4, we consider the physical origin of steep density cusps observed in the simulations with the cutoff.

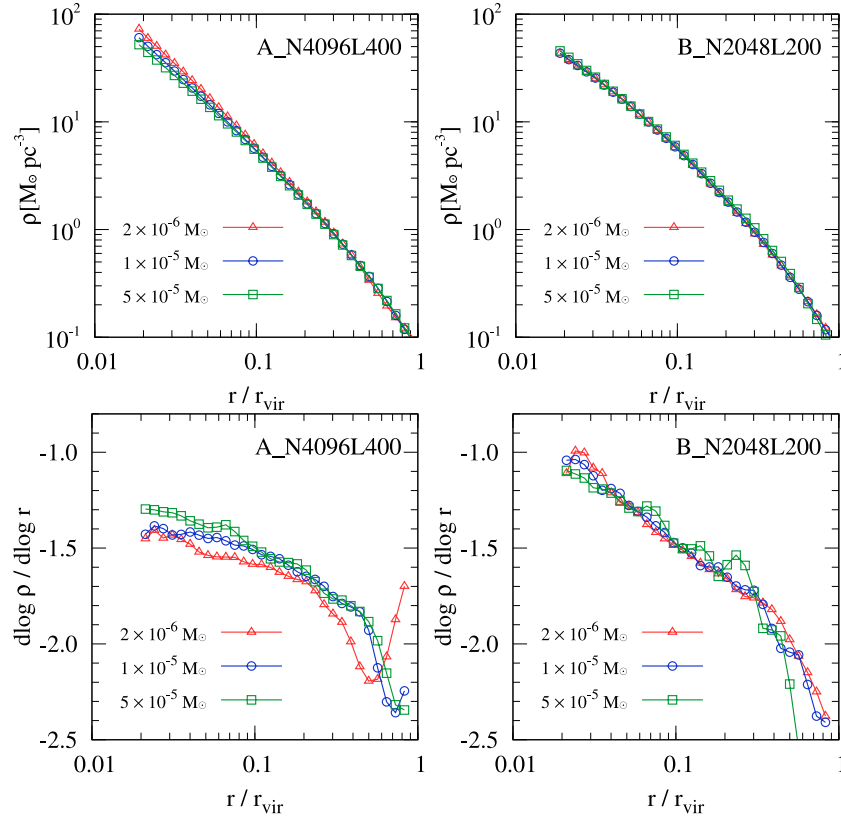


Figure 4. Stacked radial density profiles (top panel) and slope of profile (bottom panel) for A_N4096L400 and B_N2048L200 simulations as a function of radius (normalized by the virial radius).

(A color version of this figure is available in the online journal.)

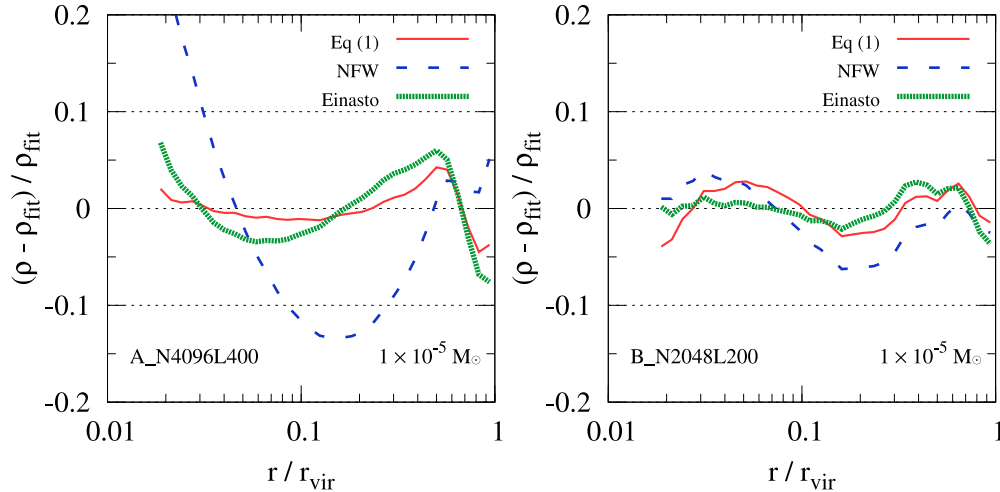


Figure 5. Residuals of stacked radial density profiles obtained from the simulations, relative to the three fitting functions.

(A color version of this figure is available in the online journal.)

3.2. Fitting Microhalo Density Profiles

3.2.1. Shape of the Inner Density Profiles

To quantify the simulated density structures, we fitted the density profiles to fitting functions. Two popular functions used in high-resolution cosmological simulations are the NFW and the Einasto profiles. In these fitting functions, the central slope is approximately -1 or less. Therefore, whether these functions can adequately describe the density profiles obtained in the simulations with the cutoff is uncertain.

Besides the NFW and Einasto profiles, we tried a double power law function, given by

$$\rho(r) = \frac{\rho_0}{(r/r_s)^\alpha (1 + r/r_s)^{(3-\alpha)}}. \quad (1)$$

This function, which has been fitted to density profiles in previous works (e.g., Diemand et al. 2004; Anderhalden & Diemand 2013), is identical to the NFW profile when $\alpha = 1$. Because the inner slope can vary, we expect that the density profiles obtained in the simulations with the cutoff can be precisely described by this function.

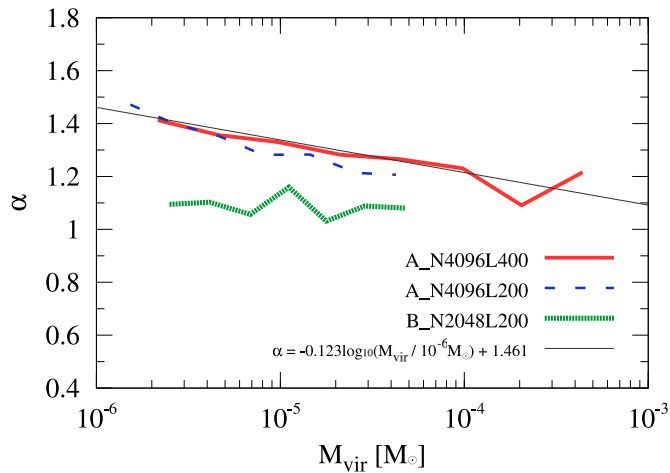


Figure 6. Slopes of stacked density profiles α as a function of the halo virial mass M_{vir} . These slopes are derived by fitting the profiles to a double power law function (Equation (1) in the text). The fittings are performed with the data divided into 32 logarithmically equal bins from $0.02r_{\text{vir}}$ to r_{vir} . Black solid line shows the best fit power law function (Equation (2) in the text).

(A color version of this figure is available in the online journal.)

As shown in Figure 5, all three of these fitting functions are well fitted to the density profiles simulated without the cutoff, consistent with previous works. The NFW profile yields a marginally worse fit than the other two functions, possibly because the other functions have an additional shape parameter α . On the other hand, the profile of the cutoff model is well-fitted only to Equation (1). As expected, the NFW profile improperly describes the density profile since it forces the central slope to be -1 . The error in the Einasto profile is acceptable, but function (1) provides a clearly superior fit. Hereafter, we use this double power function to fit the density profile obtained in simulations.

Figure 6 shows the slopes of the stacked density profiles α at $z = 32$ as functions of the halo virial mass. Only mass ranges containing more than 15 halos are plotted. As expected, the slopes are almost constant for the B_N2048L200 simulation. The value of α (~ 1.1) agrees well with that of the NFW profile. Simulations A_N4096L400 and A_N4096L200 yield very similar results. In these simulations, the slope α is considerably larger than in B_N2048L200 as seen in Figures 3 and 4. The slope difference reduces as the halo mass increases. Note that at the cutoff scale ($\sim 10^{-6} M_{\odot}$), the slope α is around 1.4–1.5, which is consistent with previous works such as Ishiyama et al. (2010, $\alpha = 1.5$) and Anderhalden & Diemand (2013, $\alpha = 1.3$ –1.4). The power law functions that best fits the relation between mass and α is

$$\alpha = -0.123 \log(M_{\text{vir}}/10^{-6} M_{\odot}) + 1.461. \quad (2)$$

This function (solid black line in Figure 6) matches the numerical results quite accurately.

To visualize the scatter in the density profiles, we fitted the profile of each halo to Equation (1) and calculated the median and scatter in each mass bin. The median, and the first and third quantiles of the shape parameter α are plotted against halo virial mass in Figure 7. The two simulations with different resolutions give similar results. The median accurately matches the fitting function derived from the stacked density profile. Regardless of halo mass, the first and third quantiles deviate by less than 20% in the A_N4096L400 simulation. Clearly,

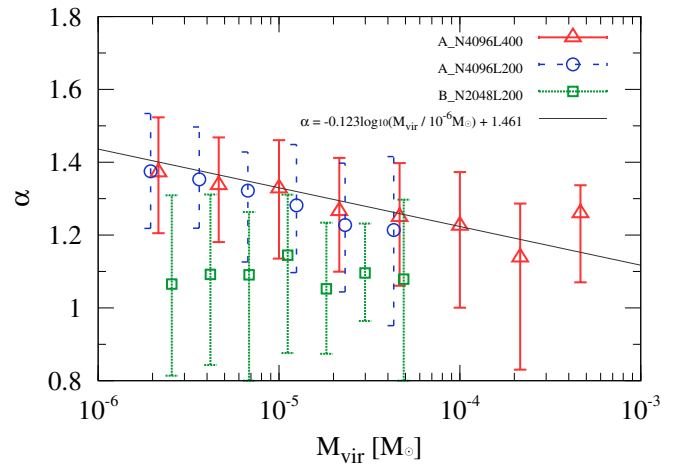


Figure 7. Slope of the density profile of each halo α plotted against the halo virial mass M_{vir} . Circles, triangles and squares show the median value in each mass bin. Whiskers are the first and third quantiles. Black solid line is the best fit power law function (Equation (2) in the text).

(A color version of this figure is available in the online journal.)

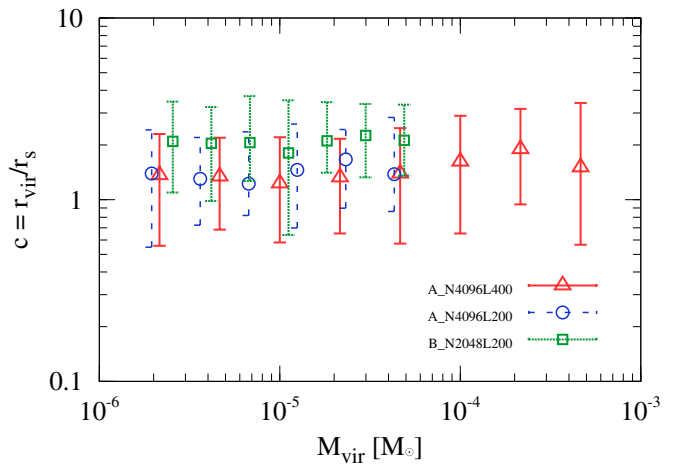


Figure 8. Concentration of the density profile of each halo r_{vir}/r_s plotted against the halo virial mass M_{vir} at $z = 32$. Circles, triangles, and squares show the median value in each mass bin. Whiskers are the first and third quantiles.

(A color version of this figure is available in the online journal.)

the B_N2048L200 simulation generates more scatter than the A_N4096L400 simulation.

3.2.2. Microhalo Concentrations

Figure 8 shows the median, first and third quantiles of the concentration parameter $c = r_{\text{vir}}/r_s$ as a function of halo virial mass. Note that the concentration parameter is defined differently than the NFW profile, since another fitting function is used. Remarkably, the concentration parameter in both models is nearly independent of halo mass over the range shown in Figure 8. The median concentration in the cutoff model is 1.2–1.7, increasing to 1.8–2.3 without the cutoff.

These results differ from what we see in larger halos (dwarf-galaxy-sized to cluster-sized halos) at lower redshifts (typically less than $z = 5$). The concentrations of these halos weakly depend on the halo mass, and have been fitted to many simple single power law functions (e.g., Neto et al. 2007). Since the slope of the power spectrum of initial density fluctuations approaches -3 for the small mass limit, the relation weakens as the halo mass decreases. There are models that connect

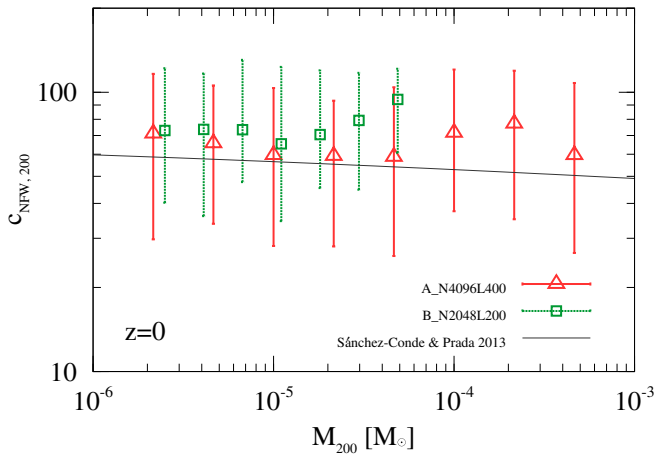


Figure 9. Converted concentration of the density profile of each halo $c_{\text{NFW},200}$ plotted against the halo mass M_{200} . The concentrations of Equation (1) are converted to those of the NFW profile at $z = 0$ as described in Section 3.2. Triangles and squares show the median value in each mass bin. Whiskers are the first and third quantiles. Black solid line is the fitting function proposed by Sanchez-Conde & Prada (2013).

(A color version of this figure is available in the online journal.)

concentrations to the rms of the linear density fluctuation field and reproduce the mass–concentration relation derived from cosmological simulations (e.g., Bullock et al. 2001; Macciò et al. 2008; Prada et al. 2012; Sanchez-Conde & Prada 2013).

Whether these fitting functions can be extrapolated to halos near the free streaming scale is worthy of investigation. Here, we present the first direct comparison using simulation results. In most previous studies, the fitting function is derived by applying the NFW profile to the simulated density profile. Our simulations robustly show that density profiles in the cutoff simulations do not follow the NFW profile and are best quantified by Equation (1). Increasing the shape parameter α would decrease the concentration by increasing the scale radius r_s . The dependence of α on the halo mass could also induce complex behavior of r_s shifts. Therefore, our results are not directly comparable with those reported elsewhere.

To enable an indirect comparison, we converted the concentration c of Equation (1) to that of the NFW profile c_{NFW} at $z = 0$ by a method adopted in previous works (e.g., Ricotti 2003; Anderhalden & Diemand 2013). For example, when $\alpha = 1.5, 1.4, 1.3$ in Equation (1), the equivalent NFW concentration $c_{\text{NFW}} = 2.0c, 1.67c, 1.43c$. Using this relation and the mass–shape relation of Equation (2), we converted the concentration in each halo mass of the cutoff simulations to its equivalent in the NFW profile. In the no cutoff simulation, where α was constant and equal to 1.1, $c_{\text{NFW}} = 1.11c$. Finally, to obtain the concentration at $z = 0$, we assumed that both the virial radius and the concentration are scalable to $z = 0$ by multiplying $(1 + z)$ (Bullock et al. 2001).

Figure 9 plots the converted concentration $c_{\text{NFW},200}$ obtained from the A_N4096L400 and B_N2048L200 simulations as a function of halo mass. In this comparison, M_{vir} and R_{vir} are replaced by the conventionally used parameters M_{200} and R_{200} , respectively, in which the spherical overdensity is 200 times the critical density. The median concentration in the cutoff model ranges 60–70. The black solid line is the function proposed by Sanchez-Conde & Prada (2013) based on the results of Prada et al. (2012). Although this fitting function can reproduce the relation between concentration and mass, it consistently underestimates the concentrations derived from the simulations.

However, the fitting lies between the first quantile and the median over more than 10 orders of extrapolation. Thus, the fitting proposed by Sanchez-Conde & Prada (2013) does not disagree with our results either qualitatively or quantitatively. The toy models of Bullock et al. (2001) and Macciò et al. (2008) give similar values. However, when simple single power law functions are extrapolated to microhalo scales (e.g., Springel et al. 2008b), the resulting concentrations are ~ 1000 , approximately one order of magnitude higher than those yielded by numerical simulations and the resulting annihilation boost factors are too high by large factors (as shown in Sanchez-Conde & Prada 2013). Our statistical studies of halos near the cutoff scale robustly show that a single power law function cannot be reliably extrapolated to this scale.

Previously, we simulated microhalos with masses of the order of $10^{-6} M_{\odot}$ (Ishiyama et al. 2010), obtained a concentration $c_{\text{NFW},200} = 60\text{--}70$. Very similar median concentrations were obtained in the present study. Other simulation of microhalo with masses of the order of $10^{-7} M_{\odot}$, (Anderhalden & Diemand 2013) yielded $c_{\text{NFW},200} = 94\text{--}124$. Although these concentrations exceed the median value of those obtained in our simulations, they reside between the first and third quantiles. We emphasize that the results of previous microhalo simulations, in which only a few halos were simulated (Ishiyama et al. 2010; Anderhalden & Diemand 2013), are not inconsistent with the present study.

Our results rule out single power law mass–concentration relations (e.g., Neto et al. 2007). However, our simulated concentration are slightly but systematically shifted upward from the fitting of Sanchez-Conde & Prada (2013). Whether this anomaly is caused by some limitation of the simulations (e.g., absence of the long-wave perturbations) or the accuracy of fitting, could be explored in larger box simulations.

3.3. Dependence of Density Profile on Halo Formation Epoch

In this section, we consider how the density profiles depend on the halo formation history. The halo formation epoch is conventionally defined as the time, at which the most massive progenitor of a halo gains half of its final mass. This definition is invalid for halos near the free streaming scale, since they are the smallest halos, do not have progenitors in principle. Therefore, we indicate the halo formation time by the halo collapse epoch z_{col} , the time at which a halo reaches threshold mass. We specify the threshold mass as $1.0 \times 10^{-6} M_{\odot}$, corresponding to 30,000 particles in simulation A_N4096L400. The masses of the progenitors were calculated as follows. First, we collected the unique IDs of all particles contained in each halo. We then identified these particles from their IDs in snapshots of redshifts higher than $z = 32$. For each particle set, we applied the spherically overdensity method and determined the mass of the progenitor.

To visualize how the collapse epoch influences the density profile, we further categorized the halo samples in each mass bin into four ranges of collapse epoch, $60 < z_{\text{col}}, 50 < z_{\text{col}} \leq 60$, and $40 < z_{\text{col}} \leq 50, z_{\text{col}} < 40$. Figure 10 shows the stacked density profiles and slopes at $z = 32$, were recalculated in each collapse epoch bin for halos in three different mass bins. Only groups containing more than 10 halos are shown. The smallest radii plotted in Figure 10 are the reliability limits based on the criteria proposed by Power et al. (2003). Densities inside of these limits are not plotted.

We can see that halos formed earlier are more concentrated than those formed later, and their central density is higher. This

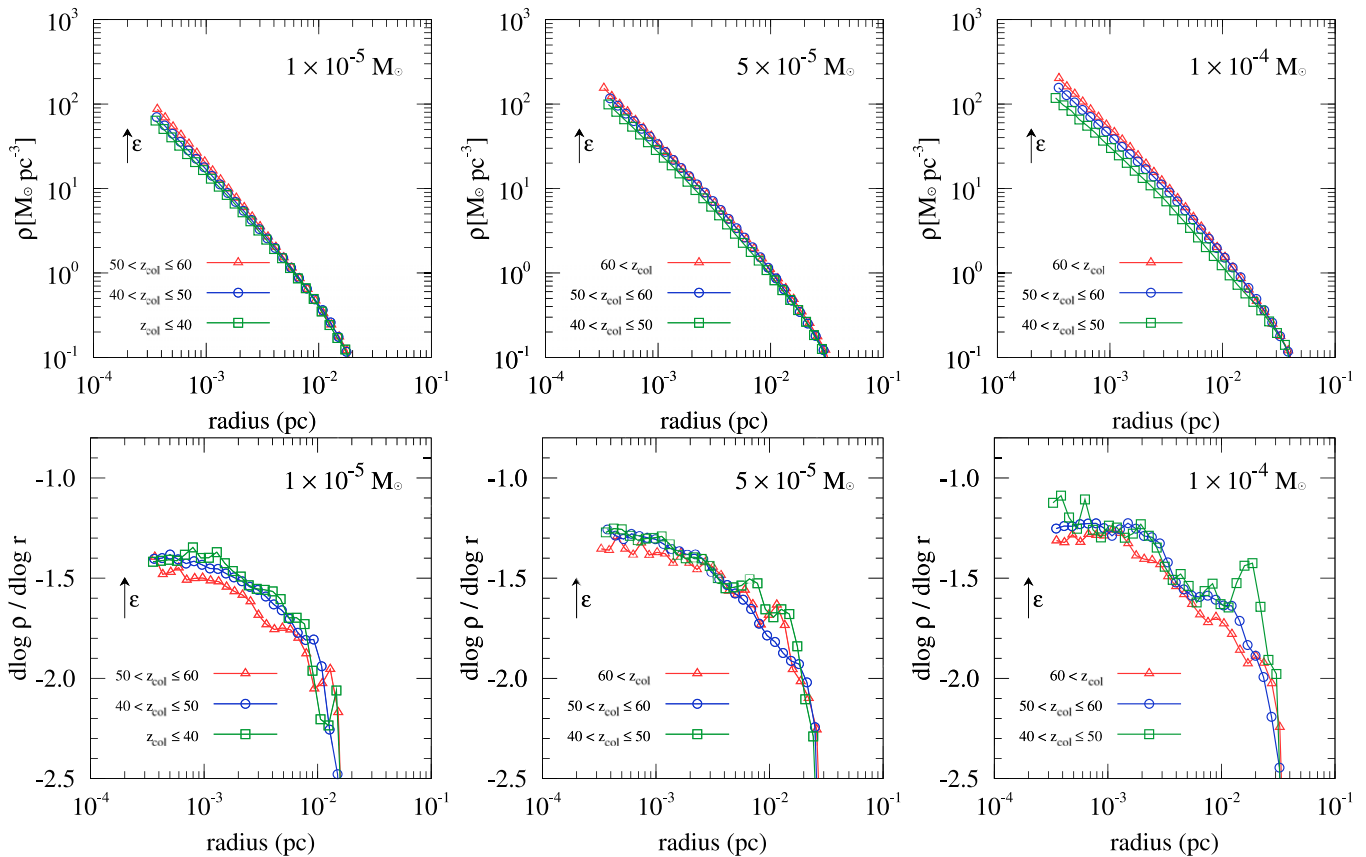


Figure 10. Stacked radial density profiles (top panel) and slopes of profiles (bottom panel) at $z = 32$ in the A_N4096L400 simulation. In each mass bin, the group of halos is categorized into several sub-groups according to the collapse epoch defined in the literature. Arrows indicate the softening length ε .

(A color version of this figure is available in the online journal.)

figure reinforces the fact that a halo concentration reflects the cosmic density at its formation time (e.g., Bullock et al. 2001).

The slopes of the density profiles appear to slightly depend on the collapse epoch. Regardless of their mass, halos with the highest collapse epochs have slightly steeper cusps than other halos, particularly at the inner regions. The inner profiles of halos with second and third highest collapse epochs are similar although their central densities differ. However, since the halos with the largest collapse epoch are rare at all halo masses, we cannot reliably infer that the slope depends on the collapse epoch. Nonetheless, we can state that the slope and the collapse epoch are not strongly correlated, therefore, the halo collapse epoch does not largely determine the shape of the density profile.

3.4. Origin of Density Profiles

No confident physical explanation exists for the formation of structures like the NFW profile found in cosmological simulations. The physical process that make steeper cusps in the smallest microhalos is also unclear. The density structures of the smallest microhalos probably deviate from the NFW because their formation processes differ from those of larger halos. In principle, the smallest halos contain no subhalos, and are not hierarchically structured from smaller constituents. Larger halos form through repeated mergers of smaller halos. We sought physical interpretation of the steep cusps in the smallest halos, but the solution eluded us at present. Nevertheless, it is worthwhile to seek the physical process that the slopes of inner cusps gradually shallow as the halo accumulates mass.

We focus on the evolution of density profiles of halos, using the samples introduced in Section 3.3. Figure 11 shows the evolution of six stacked density profiles with different collapse epochs and masses. In all samples, the cusps are clearly steeper shortly after the collapse epochs than at $z = 32$. The central slopes at the collapse are approximately -1.5 , comparable to those of the smallest microhalos in Ishiyama et al. (2010), Figures 3, 4, 6, and 7. Both central and outer densities gradually increase with decreasing redshift. The central densities grow rather more moderately as than the outer densities.

In halos with $50 < z_{\text{col}} \leq 60$, the central densities and slopes have almost ceased growing before $z = 40$. From $z = 50$ to 40 , the central slopes dramatically evolve. Differences among the profiles in each mass bin are already evident at $z = 40$. The cusps of halos with higher final mass are shallower than those of lower-mass halos. From $z = 40$ to 32 , the central densities and slopes appear to approach constant values. On the other hand, the outer densities continue to grow beyond $z = 40$, as external dark matter smoothly accretes in the outer halo regions.

Such trends also emerge in halos with $40 < z_{\text{col}} \leq 50$. Although halos with $60 < z_{\text{col}}$ display the clearest trends, the number of halos in this category is only sufficient for $1.0 \times 10^{-4} M_{\odot}$ halos. These figures indicate a non self-similar evolution of the density structure. By contrast, galaxy-sized and cluster-sized halos develop in a self-similar way (e.g., Fukushige & Makino 2001). In principle, the fraction of major mergers in halos near the free streaming scale is larger than that in larger halos because of the absence of smaller subhalos. On the other hand, major merger simulations of two isolated halos

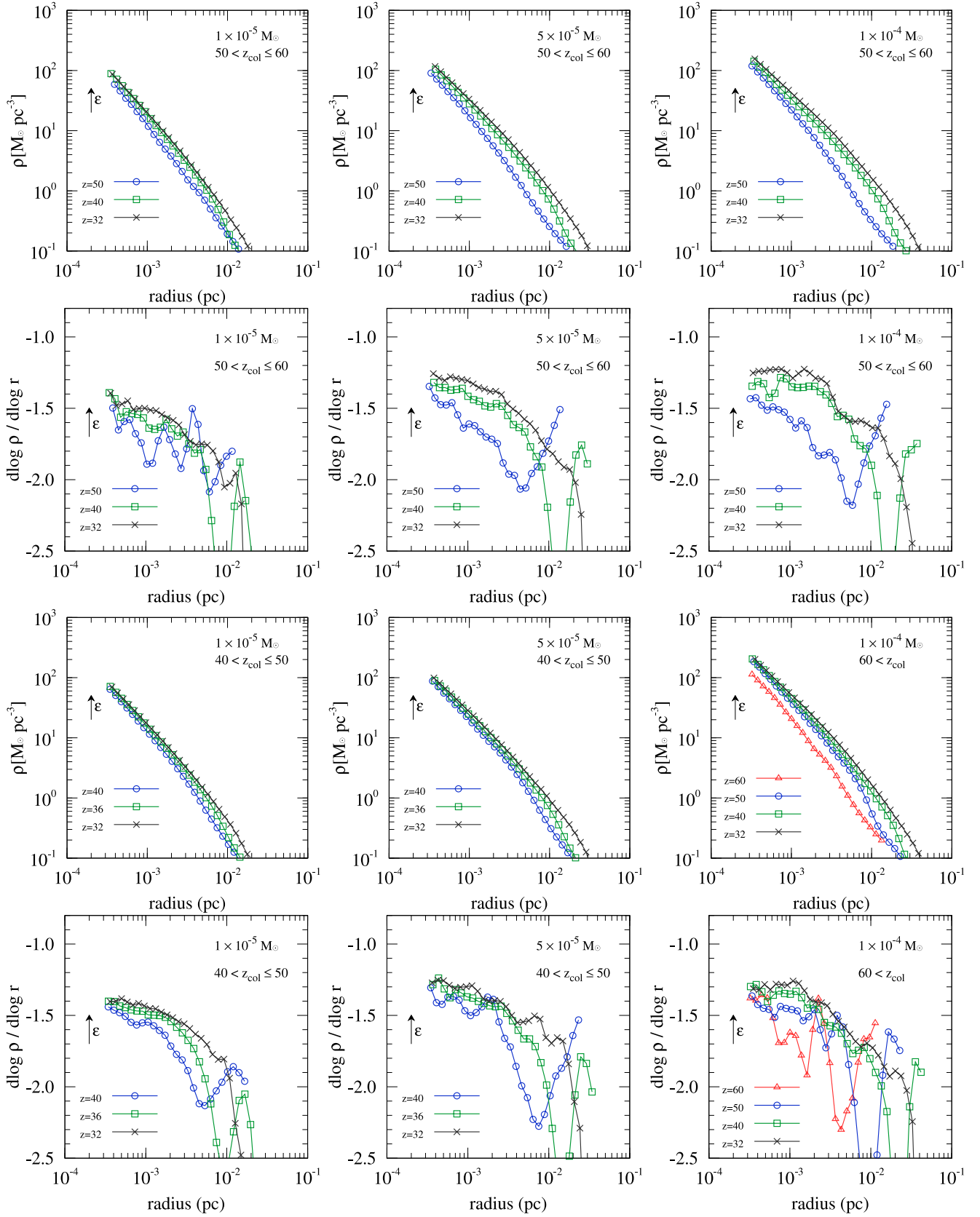


Figure 11. Evolution of the stacked radial density profiles (top panel) and slopes of profiles (bottom panel) in the A_N4096L400 simulation. Arrows indicate the softening length ϵ .

(A color version of this figure is available in the online journal.)

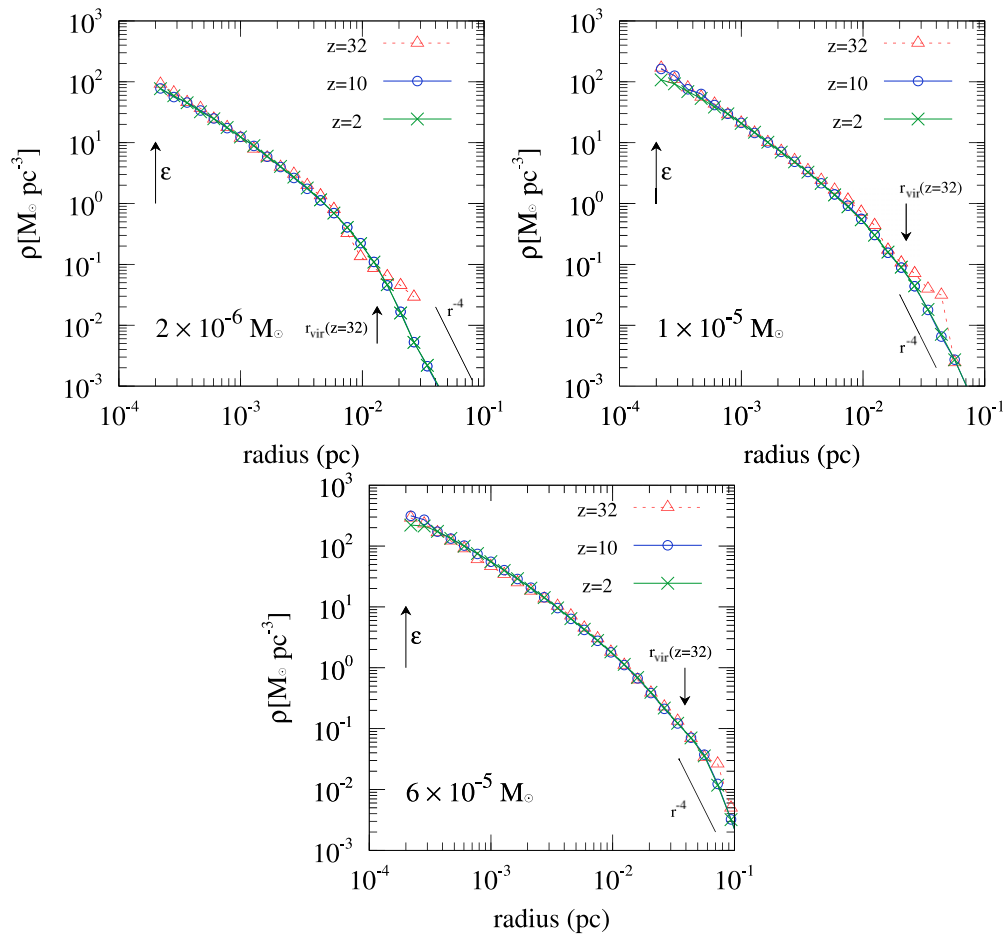


Figure 12. Evolution of density profiles toward low redshifts. Arrows indicate the softening length ϵ and the halo virial radius at $z = 32$, $r_{\text{vir}}(z = 32)$. (A color version of this figure is available in the online journal.)

showed that the steeper cusp is preserved (e.g., Boylan-Kolchin & Ma 2004; Zemp et al. 2008), consistent with a theoretical model (Dehnen 2005), or slightly reduced inner slope emerges (e.g., Boylan-Kolchin & Ma 2004). Therefore, repeated and nearly simultaneous major mergers would majorly contribute to shallowing the cusp slope in halos near the free streaming scale.

3.5. Stability of the Density Profile

One may ask whether the density structures in the simulations of the cutoff model have not stabilized. Are these density profiles with steep cusps transient? Do they transit to shallower cusps as seen in the profile of the B_N2048L200 simulation? To address these questions, we performed additional simulations to follow the evolution of these density structures.

We randomly selected three halos at $z = 32$ and evolved them as isolated systems. We extracted a $2 \times 10^{-6} M_{\odot}$ halo from then A_N4096L200 simulation, and two halos of masses $1 \times 10^{-5} M_{\odot}$ and $6 \times 10^{-5} M_{\odot}$ from the A_N4096L400 simulation. We identified particles within $2r_{\text{vir}}$ of the potential minima of these halos and re-simulated the evolution using only the tree part of GreeM code (Ishiyama et al. 2009a; Ishiyama et al. 2012) from $z = 32$ to 2. The corresponding time interval is about 3.2 Gyr. In all simulations, the constant softening value 2×10^{-4} pc was used and the opening angle for the tree method was 0.5. The properties of these halos are summarized in Table 2.

Figure 12 plots the evolution of density structures of these halos. The density structures are clearly stable from a few

Table 2
Details of Additional Simulations

N ($< r_{\text{vir}}$)	N ($< 2r_{\text{vir}}$)	m (M_{\odot})	M_{vir} (M_{\odot})	r_{vir} (pc)	Simulation
532713	1128383	4.3×10^{-12}	2.29×10^{-6}	1.32×10^{-2}	A_N4096L200
339918	694313	3.4×10^{-11}	1.16×10^{-5}	2.26×10^{-2}	A_N4096L400
1737815	3239747	3.4×10^{-11}	5.94×10^{-5}	3.92×10^{-2}	A_N4096L400

Notes. Here, $N(< r_{\text{vir}})$, $N(< 2r_{\text{vir}})$, m , M_{vir} , and r_{vir} are the number of particles within r_{vir} and $2r_{\text{vir}}$, the mass resolution, and the virial mass, and the virial radius of each halo, respectively. The last column indicates the base simulation. In all simulations, the gravitational softening length was 2×10^{-4} pc.

ϵ to r_{vir} . Beyond r_{vir} , the outskirts of all halos expand and the density profile appears to follow $\rho(r) \propto r^{-4}$, because the outskirts of each original halo was confined within $2r_{\text{vir}}$. When a halo suddenly loses its outskirts, it experiences strong gravitational disturbance and establishes a new equilibrium state. This situation naturally leads to $\rho(r) \propto r^{-4}$ (e.g., Jaffe 1987; Makino et al. 1990). However, this scenario may be unrealistic in the cosmological context, since continuous infall of matter and intermittent merger processes occur, which would increase the densities in outer regions.

Around ϵ , slight density decreases are observed at $z = 2$. These decreases are obviously numerical artifacts introduced by two-body relaxation. Therefore, the density structures with steep cusps appear to be stable rather than transient, and exist in an equilibrium state.

From these results, we can infer how these halos born in the early universe exist at present. If these halos remain sufficiently isolated from larger systems, they should wander throughout the universe while retaining their steep cusps. If captured by larger systems and exist as subhalos, their densities will be altered by tides from the larger systems. Since tidal mass loss mainly occurs in the outer regions (Diemand et al. 2007b), the high central density of these halos would remain after captured by the larger system.

Finally, what subhalo mass function can we observe in a halo as massive as the Milky Way halo? In high-resolution simulations of such halos, the mass function appeared to scale as $dn/dm \propto m^{-(2-1.8)}$, although this trend is not conclusive (e.g., Berezhinsky et al. 2003; Ishiyama et al. 2009b). However, none of previous simulations could resolve the free streaming scale, since earth mass halos are smaller than Milky Way mass halos by 18 orders of magnitude. Subhalos resolved in previous simulations have similar density structures to those of their host halo. Since these subhalos are much larger than the CDM cutoff scale, single slope in their mass function is expected. However, whether similar mass functions apply to halos near the cutoff scale is unclear, since the cusp in halos near the free streaming scale are steeper than those in larger halos.

In the A_N4096L400 simulation, more than thirty halos contained than 10 million particles at $z = 32$, sufficient for analyzing the mass function and the spatial distribution of subhalos. The statistics of these subhalos will be presented elsewhere.

4. DISCUSSIONS

4.1. Contributions of Halos Near the Free Streaming Scale to Gamma-ray Annihilation Signals

The gamma-ray luminosity of a halo by neutralino self-annihilation seen from a distant observer is calculated by the volume integral of the density squared. Any subhalos boost the annihilation luminosity of a halo and the boost factor $B(M)$ is defined as (e.g., Strigari et al. 2007)

$$B(M) = \frac{1}{L(M)} \int_{M_{\min}}^M \frac{dn}{dm} [1 + B(m)] L(m) dm, \quad (3)$$

where, $L(M)$ is the annihilation luminosity of a halo of mass M without subhalos, and $dn/dm = A/M(m/M)^{-\zeta}$ is the subhalo mass function.

The boost factor of a Milky-Way-sized halo has been estimated by many studies and ranges from a few to several tens (e.g., Colafrancesco et al. 2006; Diemand et al. 2007a, 2008; Kamionkowski et al. 2010; Kuhlen et al. 2012; Sanchez-Conde & Prada 2013). Some works give several hundreds (Springel et al. 2008b).

In many early studies, annihilation luminosities and boost factors, have been evaluated assuming that halos near the free streaming scale follow the NFW profile. The steeper cusps obtained in our simulations could significantly enhance the signals. In this section, we evaluate boost factors using the density profiles obtained in our simulations. However, many uncertainties, the evolution of these halos in the Milky Way, subhalo mass function, and the profile of the Milky Way halo, weaken the reliability of estimation. Nevertheless, such estimation is worthy to attempt and gives us some insights about the boost factor.

As models of halos near the free streaming scale, we consider three models.

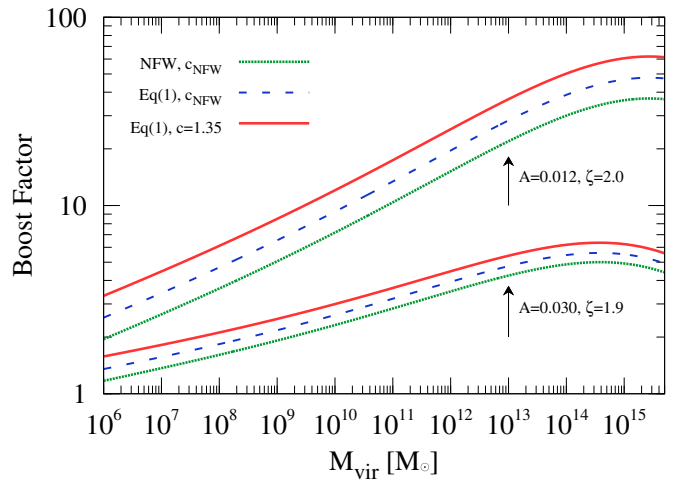


Figure 13. Annihilation boost factor as a function of the halo mass. The results of three models of halos near the free streaming scale are shown. The subhalo mass function $dn/dm = 0.012/M(m/M)^{-2.0}$ gives upper three curves. The subhalo mass function $dn/dm = 0.030/M(m/M)^{-1.9}$ gives lower three curves.

(A color version of this figure is available in the online journal.)

1. *EQ1_c1p35*. The profile of Equation (1) with the mass–shape relation of Equation (2), and the constant concentration $c = 1.35$ at $z = 32$, consistent with our cutoff simulation.
2. *EQ1_cNFW*. The profile of Equation (1) with the mass–shape relation of Equation (2), and the mass–concentration relation proposed by Sanchez-Conde & Prada (2013). This NFW concentration is converted to that of Equation (1) by the way described in Section 3.2.2.
3. *NFW_cNFW*. The NFW profile and the mass–concentration relation proposed by Sanchez-Conde & Prada (2013).

In the mass–shape relation of Equation (2), the inner shape becomes $\alpha = 1$ at the mass $\sim 5.6 \times 10^{-3} M_{\odot}$. We assume that the density profile is identical to the NFW profile above this mass scale. We used the subhalo mass function of $\zeta = 1.9$ and 2.0, corresponding normalization factors are $A = 0.03$ and 0.012 (e.g., Sanchez-Conde & Prada 2013) and calculated the annihilation luminosity of each mass halo by numerically integrating the square of Equation (1) within the range 10^{-5} pc to r_{vir} , with the parameters of adopted model. Then the boost factor was calculated by numerically integrating Equation (3) from $M_{\min} = 10^{-6} M_{\odot}$ under the condition $B(M_{\min}) = 0$.

Figure 13 shows the annihilation boost factor as a function of the halo mass. The result of NFW_cNFW model is identical to that shown in Sanchez-Conde & Prada (2013). The models with steeper inner (EQ1_c1p35 and EQ1_cNFW) raise the boost factor moderately. The model EQ1_c1p35 gives larger enhancement than the model EQ1_cNFW, since its concentrations are larger as seen in Figure 9. The boost factors of a Milky Way sized halo ($M = 2.0 \times 10^{12} M_{\odot}$) with the $\zeta = 2.0$ subhalo mass function are $\sim 17, 22$ and 29 for models of NFW_cNFW, EQ1_cNFW and EQ1_c1p35, respectively. Those with the $\zeta = 1.9$ subhalo mass function are $\sim 3.7, 4.2$ and 4.8. Strongly depending on the subhalo mass function and the adopted concentration model, the steeper inner cusps of halos near the free streaming scale enhance the annihilation luminosity of a Milky-Way-sized halo between 12% to 67%.

When simple single power law mass–concentration relations are extrapolated to microhalo scales, the resulting boost factor is several hundreds for a Milky-Way-sized halo (e.g., Springel

et al. 2008b), and ~ 1000 for a cluster-sized halo (Pinzke et al. 2011; Gao et al. 2012). Such very large boost factors are clearly ruled out as seen in Figure 13, since our high-resolution simulations rule out single power law mass–concentration relations.

The scatter in the density profiles seen in Figures 7 and 8 could influence the boost factor. To evaluate the effect of the scatter, we calculated the annihilation luminosity of each simulated halo by numerically integrating the square of Equation (1), with the parameters obtained in the fitting of each halo. We find that the average luminosity is 28% smaller than that we do not consider the scatter. Thus, the scatter in the density profiles would not cause large effect on the boost factors.

Our work has improved the accuracy of the estimation of the boost factor. However, some uncertainties still exist. It is unclear whether the subhalo mass function can be extrapolated to the scale of microhalos, since the central density cusp is steeper in these halos than in larger halos. The boost factor strongly depends on the cutoff mass scale (e.g., Anderhalden & Diemand 2013; Sanchez-Conde & Prada 2013). Further studies about the evolution of microhalos in larger halos and a cutoff scale independent model of density profiles, are required to estimate the boost factor more robustly.

4.2. Analogy with Warm Dark Matter Simulations

Our studies are closely related to warm dark matter simulations. Although mass scales are largely different, the mechanism to impose the cutoff in the matter power spectrum is similar. Thus, the structure of halos near the cutoff scale of warm dark matter particles should be similar to those obtained in our simulations.

The mass–shape relation of Equation (2) predicts that the slopes with the cutoff and no cutoff models are similar at around $10^{-3} M_\odot$, which is about three orders larger than the cutoff scale. This prediction is consistent with recent warm dark matter simulations (e.g., Anderhalden et al. 2012; Lovell et al. 2014) that gave density profiles similar to the NFW profile for the Milky Way mass halos, which are larger than the cutoff scale of warm dark matter particles by three orders of magnitude.

Our results indicate that the cusps of warm dark matter halos below the Milky Way mass would be steeper than that of the NFW profile. However, there is an absence of simulation data. Our understanding of halo structures will advance by high-resolution warm dark matter simulations, which resolve halos near its cutoff scale.

5. SUMMARY

By means of unprecedentedly large cosmological N -body simulations, we studied the structures of dark matter halos near the free streaming scale over a wide mass range ($\sim 10^{-(6-4)} M_\odot$). These simulations enable to resolve halos with sufficient resolution and cover volumes large enough to perform statistical studies. Two different initial matter power spectra were adopted, one accounting for the free streaming damping, the other ignoring this effect. We investigated the effect of the free streaming damping on structures of halos. Our main results are summarized below.

1. The central cusp of the smallest microhalos scales as $\rho \propto r^{-(1.5-1.3)}$, much steeper than that of the NFW profile, but consistent with previous works (Ishiyama et al. 2010; Anderhalden & Diemand 2013). The central cusp becomes

gradually shallower as the halo mass increases. For halos of mass $5 \times 10^{-5} M_\odot$, the central slope is around -1.3 .

2. The density profiles of these halos are not well fitted by the NFW profile, but can be fitted to a double power law function (Equation (1)). Within the mass range of this study, the shape parameter α is given as $\alpha = -0.123 \log(M_{\text{vir}}/10^{-6} M_\odot) + 1.461$.
3. The concentration parameter shows little dependence on the halo mass within the mass range of this study. The median concentration in the cutoff and the no cutoff models ranges 1.2–1.7 and 1.8–2.3, respectively, corresponding to conventional concentrations (based on the NFW profile at $z = 0$) of 60–70. These results support suggestions that the concentration does not depend on mass in a single power law fashion.
4. No strong correlation exists between the slope and the collapse epoch, indicating that halo collapse is not important in determining the shape of the density profile. The density profile does not evolve self-similarly, unlike larger halos such as galaxy-sized and cluster-sized halos. Shortly after collapse, the cusps are steeper and their profiles are similar to those of the smallest halos. The cusp slope in halos near the free streaming scale should be predominantly reduced by merger processes.
5. These density profiles with steep cusps are not transient and exist in an equilibrium state.

We thank the anonymous referee for valuable comments. Numerical computations were partially carried out on Aterui supercomputer at Center for Computational Astrophysics, CfCA, of National Astronomical Observatory of Japan, and the K computer at the RIKEN Advanced Institute for Computational Science (Proposal numbers hp120286 and hp130026). This work has been funded by MEXT HPCI STRATEGIC PROGRAM and MEXT/JSPS KAKENHI grant No. 24740115.

REFERENCES

- Anderhalden, D., & Diemand, J. 2013, *JCAP*, **04**, 009
Anderhalden, D., Diemand, J., Bertone, G., Macciò, A. V., & Schneider, A. 2012, *JCAP*, **10**, 047
Ando, S., Kamionkowski, M., Lee, S. K., & Koushiappas, S. M. 2008, *PhRvD*, **78**, 101301
Angulo, R. E., Hahn, O., & Abel, T. 2013, *MNRAS*, **434**, 3337
Belotsky, K. M., Kirillov, A. A., & Khlopov, M. Y. 2014, *Gravitation and Cosmology*, **20**, 47
Berezinsky, V., Dokuchaev, V., & Eroshenko, Y. 2003, *PhRvD*, **68**, 103003
Berezinsky, V., Dokuchaev, V., & Eroshenko, Y. 2008, *PhRvD*, **77**, 083519
Bertschinger, E. 2006, *PhRvD*, **74**, 063509
Blanchet, S., & Laval, J. 2012, *JCAP*, **11**, 021
Bode, P., Ostriker, J. P., & Turok, N. 2001, *ApJ*, **556**, 93
Boylan-Kolchin, M., & Ma, C.-P. 2004, *MNRAS*, **349**, 1117
Bryan, G. L., & Norman, M. L. 1998, *ApJ*, **495**, 80
Bullock, J. S., Kolatt, T. S., Sigad, Y., et al. 2001, *MNRAS*, **321**, 559
Charbonnier, A., Combet, C., Daniel, M., et al. 2011, *MNRAS*, **418**, 1526
Colafrancesco, S., Profumo, S., & Ullio, P. 2006, *A&A*, **455**, 21
Colín, P., Valenzuela, O., & Avila-Reese, V. 2008, *ApJ*, **673**, 203
Dehnen, W. 2005, *MNRAS*, **360**, 892
Diemand, J., Kuhlen, M., & Madau, P. 2006, *ApJ*, **649**, 1
Diemand, J., Kuhlen, M., & Madau, P. 2007a, *ApJ*, **657**, 262
Diemand, J., Kuhlen, M., & Madau, P. 2007b, *ApJ*, **667**, 859
Diemand, J., Kuhlen, M., Madau, P., et al. 2008, *Natur*, **454**, 735
Diemand, J., Moore, B., & Stadel, J. 2004, *MNRAS*, **353**, 624
Diemand, J., Moore, B., & Stadel, J. 2005, *Natur*, **433**, 389
Einasto, J. 1965, *Trudy Astrofizicheskogo Instituta Alma-Ata*, **5**, 87
Fukushige, T., Kawai, A., & Makino, J. 2004, *ApJ*, **606**, 625
Fukushige, T., & Makino, J. 2001, *ApJ*, **557**, 533
Gao, L., Frenk, C. S., Jenkins, A., Springel, V., & White, S. D. M. 2012, *MNRAS*, **419**, 1721

- Giocoli, C., Pieri, L., Tormen, G., & Moreno, J. 2009, *MNRAS*, **395**, 1620
- Goerdt, T., Gnedin, O. Y., Moore, B., Diemand, J., & Stadel, J. 2007, *MNRAS*, **375**, 191
- Green, A. M., Hofmann, S., & Schwarz, D. J. 2004, *MNRAS*, **353**, L23
- Hofmann, S., Schwarz, D. J., & Stöcker, H. 2001, *PhRvD*, **64**, 083507
- Ishiyama, T., Fukushige, T., & Makino, J. 2009a, *PASJ*, **61**, 1319
- Ishiyama, T., Fukushige, T., & Makino, J. 2009b, *ApJ*, **696**, 2115
- Ishiyama, T., Makino, J., & Ebisuzaki, T. 2010, *ApJL*, **723**, L195
- Ishiyama, T., Nitadori, K., & Makino, J. 2012, in Proc. Int. Conf. High Performance Computing, Networking, Storage and Analysis, SC '12 (Los Alamitos, CA: IEEE Computer Society Press), 5, (arXiv:1211.4406)
- Ishiyama, T., Rieder, S., Makino, J., et al. 2013, *ApJ*, **767**, 146
- Jaffe, W. 1987, in IAU Symp. 127, Structure and Dynamics of Elliptical Galaxies, ed. P. T. de Zeeuw & S. D. Tremaine (Cambridge: Cambridge Univ. Press), 511
- Kamionkowski, M., Koushiappas, S. M., & Kuhlen, M. 2010, *PhRvD*, **81**, 043532
- Komatsu, E., Smith, K. M., Dunkley, J., et al. 2011, *ApJS*, **192**, 18
- Koushiappas, S. M. 2006, *PhRvL*, **97**, 191301
- Koushiappas, S. M., Zentner, A. R., & Walker, T. P. 2004, *PhRvD*, **69**, 043501
- Kuhlen, M., Diemand, J., & Madau, P. 2008, *ApJ*, **686**, 262
- Kuhlen, M., Vogelsberger, M., & Angulo, R. 2012, *PDU*, **1**, 50
- Lacey, C., & Cole, S. 1994, *MNRAS*, **271**, 676
- Lee, S. K., Ando, S., & Kamionkowski, M. 2009, *JCAP*, **07**, 007
- Loeb, A., & Zaldarriaga, M. 2005, *PhRvD*, **71**, 103520
- Lovell, M. R., Frenk, C. S., Eke, V. R., et al. 2014, *MNRAS*, **439**, 300
- Macciò, A. V., Dutton, A. A., & van den Bosch, F. C. 2008, *MNRAS*, **391**, 1940
- Mack, K. J. 2014, *MNRAS*, **439**, 2728
- Makino, J., Akiyama, K., & Sugimoto, D. 1990, *PASJ*, **42**, 205
- Navarro, J. F., Frenk, C. S., & White, S. D. M. 1996, *ApJ*, **462**, 563
- Neto, A. F., Gao, L., Bett, P., et al. 2007, *MNRAS*, **381**, 1450
- Ng, K. C. Y., Laha, R., Campbell, S., et al. 2013, *PRD*, **89**, 8
- Nitadori, K., Makino, J., & Hut, P. 2006, *NewA*, **12**, 169
- Oda, T., Totani, T., & Nagashima, M. 2005, *ApJL*, **633**, L65
- Pieri, L., Lavalle, J., Bertone, G., & Branchini, E. 2011, *PhRvD*, **83**, 023518
- Pinzke, A., Pfrommer, C., & Bergström, L. 2011, *PhRvD*, **84**, 123509
- Power, C., Navarro, J. F., Jenkins, A., et al. 2003, *MNRAS*, **338**, 14
- Prada, F., Klypin, A. A., Cuesta, A. J., Betancort-Rijo, J. E., & Primack, J. 2012, *MNRAS*, **423**, 3018
- Profumo, S., Sigurdson, K., & Kamionkowski, M. 2006, *PhRvL*, **97**, 031301
- Ricotti, M. 2003, *MNRAS*, **344**, 1237
- Sanchez-Conde, M. A., & Prada, F. 2013, arXiv:1312.1729
- Schneider, A., Krauss, L., & Moore, B. 2010, *PhRvD*, **82**, 063525
- Schneider, A., Smith, R. E., & Reed, D. 2013, *MNRAS*, **433**, 1573
- Springel, V., Wang, J., Vogelsberger, M., et al. 2008a, *MNRAS*, **391**, 1685
- Springel, V., White, S. D. M., Frenk, C. S., et al. 2008b, *Natur*, **456**, 73
- Stadel, J., Potter, D., Moore, B., et al. 2009, *MNRAS*, **398**, L21
- Strigari, L. E., Koushiappas, S. M., Bullock, J. S., & Kaplinghat, M. 2007, *PhRvD*, **75**, 083526
- Tanikawa, A., Yoshikawa, K., Nitadori, K., & Okamoto, T. 2013, *NewA*, **19**, 74
- Tanikawa, A., Yoshikawa, K., Okamoto, T., & Nitadori, K. 2012, *NewA*, **17**, 82
- Wang, J., & White, S. D. M. 2007, *MNRAS*, **380**, 93
- Zemp, M., Moore, B., Stadel, J., Carollo, C. M., & Madau, P. 2008, *MNRAS*, **386**, 1543
- Zybin, K. P., Vysotsky, M. I., & Gurevich, A. V. 1999, *PhLA*, **260**, 262